

# Two-dimensional spectroscopic observations of chromospheric oscillations

Nurol Al<sup>1</sup>, Cornelia Bendlin<sup>2</sup>, and Franz Kneer<sup>3</sup>

<sup>1</sup> Istanbul Üniversitesi, Üniversite Rasathanesi, 34452 Üniversite-Istanbul, Turkey

<sup>2</sup> Astronomisches Institut der Universität Würzburg, Am Hubland, D-97074 Würzburg, Germany

<sup>3</sup> Universitäts-Sternwarte Göttingen, Geismarlandstrasse 11, D-37083 Göttingen, Germany

Received 23 December 1997 / Accepted 27 April 1998

**Abstract.** The oscillatory behaviour of the solar chromosphere was studied from observations of a quiet region at disk centre using various diagnostic tools. The two-dimensional spectrometer in the Vacuum Tower Telescope/Tenerife (Spain) served to obtain a spatially highly resolved time series of “white-light” images and narrow-band filtergrams in the Na D<sub>2</sub> line. With a tunable Fabry-Perot interferometer, this line was scanned taking 30 images (i.e. a “scan”) around the line core with wavelength steps of 30 mÅ and a spectral resolution of about 200 000. From these images, line profiles were derived for every pixel in the field of view. With each such narrow-band scan, a scan of “white-light” images was taken strictly simultaneously. The whole time series comprises (2 ×) 128 scans. Every 56 s, a new pair of scans was started with two CCDs, thus the observation covers nearly two hours. Finally, after correlation and other reduction procedures, a field size of 69′.4 × 50′.4 remained with 0′.2/pixel on the CCD-chips. In the data reduction, new images were created representing the minimum intensity (I) of each line profile in the field of view, and also velocity (V) maps (derived from the Doppler shifts of the line profiles) for all 128 scans. From these images, power spectra and diagnostic diagrams were computed. In the subsequent analysis, a distinction between network and intra-network regions was made where this seemed appropriate. One- and two-dimensional (V–I) phase and coherence spectra were analysed with regard to oscillations and to the nature of the waves leaving their marks in these diagrams. Several noteworthy results also raised the question of the actual line formation height of Na D<sub>2</sub>, among them being the non-detection of a chromospheric eigenmode. While an explanation for a conspicuous 70° plateau in a small region of the phase spectra already exists, the suspected reason behind the decreasing phase difference from about –60° for the f-mode down to ~ –120° for higher modes is still subject to some speculation. Moreover, the data gave evidence of gravity waves, probably discovered for the first time in a V–I phase spectrum of Na D<sub>2</sub>.

**Key words:** Sun: chromosphere – Sun: oscillations – techniques: spectroscopic

## 1. Introduction

Oscillations in the solar photosphere and chromosphere had already been postulated about 50 years ago (Schwarzschild 1948), but it was not until the beginning of the 1960s (Leighton et al. 1962) that the first observational proof of their existence followed. Despite many successful attempts from theory and observation to further clarify their origin and the nature of the waves involved (e.g. Ulrich (1970) and Deubner (1975)), the oscillatory behaviour of the solar atmosphere still defies a fully satisfactory explanation. The persistent question of the heating of the solar chromosphere and corona also keeps calling for further efforts in this field.

No final answers to the challenge outlined above can be given here, but this paper contributes new observational results to this end. Some unexpected findings from two-dimensional observations obtained with high spatial resolution in the Na D<sub>2</sub> line offer new aspects which will have to be considered in the ongoing discussion about chromospheric oscillations.

## 2. Observations

### 2.1. General overview

On May 25, 1995, a time series of a quiet region at the centre of the solar disk was taken with the Vacuum Tower Telescope (VTT) at the Observatorio del Teide on Tenerife. For this observation, the two-dimensional spectrometer mounted in an optical laboratory of the VTT (see e.g. Bendlin et al. (1992)) was used to obtain so-called white-light images and narrow-band filtergrams in the Na D<sub>2</sub> line strictly simultaneously with two CCDs. Its line formation height makes Na D<sub>2</sub> a suitable tool for studying the lower to middle chromosphere.

### 2.2. Short introduction to the two-dimensional spectrometer

As the spectrometer in the VTT is a non-standard and also a versatile instrument meeting different observational needs (Volkmer 1995), a mere description of the observations gained with it will not provide sufficient information on the peculiarities of the data and their proper treatment in the reduction. A schematic representation as well as a detailed description of the spectrometer is

given in Bendlin et al. (1992), while some components which were introduced more recently are treated in Bendlin & Volkmer (1995).

For two-dimensional spectroscopic observations, like here, the instrumental set-up mainly consists of a series of filters placed in the light path leading to “CCD 2” which is used to take narrow-band filtergrams. First, an interference filter (IF) with a FWHM of about  $10 \text{ \AA}$  was chosen to pre-select the wavelength range around the  $\text{Na D}_2$  line. A beam splitter cube (BSC) behind the IF reflects some light onto “CCD 1” which thus receives so-called white light, but about 90% of the transmitted light passes the BSC in the direction of CCD 2. The IF also serves to suppress neighbouring maxima in the transmission curve of the next filter. The latter is a universal birefringent filter (UBF) with a FWHM of  $0.46 \text{ \AA}$  at the wavelength of  $\text{Na D}_2$  ( $5890 \text{ \AA}$ ). A considerably narrower pass band is produced by a Fabry-Perot interferometer (FPI), the last filter in line. Specific information on the FPI used here and on the relevant formulae describing its performance can be found (e.g.) in Bendlin (1993) or Bendlin & Volkmer (1995), therefore only such characteristics are mentioned here which are essential in this context. The FPI’s spectral resolution (and wavelength position of the selected transmission maximum) is variable, depending on the separation of its mirror plates. For the rather broad  $\text{Na D}_2$  line, a mirror gap  $d$  of  $1.25 \text{ mm}$  yielding a spectral resolution of about  $2 \times 10^5$  was considered an acceptable compromise, as the free spectral range  $\text{FSR} \propto d^{-1}$  thus becomes wide enough ( $1.38 \text{ \AA}$ ) for scanning through a sufficiently large part of the line. The performance of the FPI is determined by a computer-controlled ramp generator feeding the piezoelectric stacks of one mirror with the required voltage to alter the mirror separation in a well-defined way. The images within a scan were taken in quick succession. After each individual exposure, the pass band of the FPI was shifted by  $30 \text{ m\AA}$ . This procedure was repeated from the beginning of the selected wavelength range for every scan of the time series.

The UBF is placed at a telecentric position, thus the transmission conditions for the different light bundles belonging to different points in the field of view are uniform. The same cannot be said of the FPI which leaves all *parallel* rays of light, belonging to any one point, with a blueshift due to its position at the pupil’s image of the telescope. The blueshift is largest for the largest angles of incidence and vanishes for rays parallel to the optical axis. This effect is taken into account (and corrected for in the data reduction), as the FPI’s position at the pupil’s image guarantees the highest spectral resolution possible.

Two personal computers (PCs) execute the specific observational programme defined by suitably chosen observing parameters which are entered via a special software control programme. The Peltier-cooled CCDs connected with these PCs take images with a resolution of 12 bits. The maximum image acquisition rate is better than 3 full frames (corresponding to  $384 \times 286$  pixels) per second. While a scan is taken, the CCD frames are stored in the PC-RAM, and in between two successive scans the data are transferred onto a hard disk.

When needed, several additional light paths branching off or leading into the main light path may be utilized via movable mirrors. Of foremost importance is the light path containing a *continuum source* to take flat-field images spanning the same wavelength range as the solar images in order to obtain “pure” transmission curves under the same conditions as the actual time series. It was therefore designed to imitate the solar light path as closely as possible to ensure that the same angles of incidence occur on the various optical surfaces of the spectrometer’s components and that the same blueshifts of the transmission curves are produced by the FPI.

Some other light paths are equipped with helpful components to facilitate any necessary adjustments of the spectrometer.

### 2.3. Outline of the observations

From the wide range of observing parameters offered by the instrumental set-up and the software programme controlling the spectrometer, the following combination was chosen for the observed set of data:

The number of white-light and narrow-band scans in the time series is 128, each made up of 30 individual CCD frames. Every 56 s, a new scan was started, so the whole time series covers nearly two hours. With the selected mirror separation of the FPI, the spectral resolution reached about  $2 \times 10^5$ , corresponding to a smallest resolvable wavelength difference of  $\sim 30 \text{ m\AA}$ . The wavelength step between successive narrow-band images was  $30 \text{ m\AA}$  as well. For solar images (and, of course, the corresponding dark and flat-field images), an exposure time of 60 ms proved sufficient. In order to obtain solar flat-field scans, the telescope was defocused. The flat-field images taken with a continuum source, necessary for the narrow-band scans only, reached a fair signal-to-noise ratio after an integration time of 600 ms. They required another set of dark images with the same exposure time. With the CCDs’ maximum field of view of  $384 \times 286$  pixels and with the imaging achromat used here, a spatial resolution of  $0''.2$  per pixel on the CCD-chips was achieved, yielding an (original) image size of  $76''.8 \times 57''.2$ .

The whole set of data necessary for the data reduction was supplemented with so-called grid images. They were taken after the final adjustment of the spectrometer with a grid placed at the prime focus of the VTT. These exposures are needed for the correct alignment of white-light images with the narrow-band filtergrams (see Sect. 3.1).

## 3. Data reduction

The essential steps to be performed in the data reduction have minutely been described in a thesis (Al 1997), and many of them also in Bendlin & Volkmer (1995), but there is no comprehensive overview readily available. The unusual and complex problems arising from the data obtained with the two-dimensional spectrometer therefore suggest a somewhat abridged, yet sufficiently detailed description here.

### 3.1. Preparatory steps

Among the *narrow-band* images which differ considerably within a scan, neither a correlation nor a “destretching” algorithm will work satisfactorily, therefore the results of both have to be derived from the white-light images first and must afterwards be applied to the narrow-band images taken strictly simultaneously. As a necessary prerequisite for this procedure, the common field of view must have been determined from the images of CCD 1 and CCD 2. After proper preparation, the grid images taken for this purpose revealed slightly different imaging ratios which entailed a reduction of the field of view for all white-light images. Finally, the distortions induced by the optical components characteristic of the light path leading to CCD 1 (as compared to the CCD 2-images) were removed using a destretching programme. With the information gained by the reduction steps performed with the grid images, everything was prepared for the subsequent alignment of the white-light with the narrow-band images.

### 3.2. White-light images

After subtraction of an averaged dark image from every raw white-light image, the solar images were divided by an averaged flat-field image. (Here, “averaged” always refers to the mean values for the individual pixels.) The field of view of the solar images was slightly reduced to match the imaging ratio of the narrow-band filtergrams, and the frames were all “cut” to their common image size. Then, the destretching coefficients obtained from the destretching algorithm used to compare the grid images of CCD 1 and CCD 2 were applied to all white-light images. After that, the rms value of the intensity was calculated for every image, and the “best” (or “reference”) white-light image defined by the highest rms value within each scan was determined and stored separately. Despite the short exposure time and the fairly high image acquisition rate it proved necessary to correlate the images within each scan with their corresponding reference image to correct for image motion. The resulting shifts were first applied to the individual white-light images. Afterwards, the same procedure could be repeated with the corresponding narrow-band filtergrams taken simultaneously (see Sect. 3.3). Apart from image motion, seeing-induced distortions had to be compensated for by cross-correlation as well. Again, the destretching coefficients determined (and used) here were also valid for the narrow-band filtergrams and were thus kept for subsequent reduction steps. Noise was reduced in both spatial dimensions of the white-light data via an optimum filter working in the Fourier domain.

After the correlation of all images within each of the 128 scans making up the time series, the 128 reference images still had to be correlated with each other because of the “residual” image motion shifting “whole scans” against each other. By this procedure, the possible occurrence of guiding errors of the telescope was also taken into account. Next, the same correlation as for their corresponding reference image was performed for the other images in each scan as well, after which the common

image size in all ( $128 \times 30$ ) frames was found to be  $357 \times 262$  pixels or  $71''.4 \times 52''.4$ , respectively. Finally, the intensities of the reference images were normalized to make up for the increasing intensity the telescope received during the observation due to the rising Sun. Besides, the division of each reference image by the mean intensity value of its corresponding scan ensured that in case of varying transparency of the Earth’s atmosphere any resulting intensity fluctuations had also been compensated for.

### 3.3. Narrow-band filtergrams

Analogous to the reduction of the white-light images, first, the corresponding averaged dark image was subtracted from each image taken with the same exposure time. The flat-field correction, however, is quite different: In principle, every narrow-band image of each solar scan has to be divided by a flat-field image taken at exactly the same wavelength position, yet, the latter must *not* contain the Na D<sub>2</sub> line. The scan obtained with a continuum source fulfils this requirement, but these flat-field images represent a different spatial intensity pattern than a uniform solar surface would have produced. Obviously, the opposite is true of the solar flat-field scan. It therefore suggested itself to combine the advantages of both scans and eliminate their shortcomings in creating a so-called artificial flat-field scan (see Bendlin & Volkmer (1995) for details) which is “ideal” in every respect. The intensity pattern of the new scan looks as if it were obtained with uniform solar light, which means no spatial intensity variation on the Sun *and* constant intensity in the spectral range of the Na D<sub>2</sub> line. The transmission curves for each pixel on the CCD-chip thus also show the same blueshift according to their relative position to the optical axis as the line profiles contained in the narrow-band scans (apart from Doppler shifts) do. The fact that the automatic stabilization programme for the FPI allows the interferometer’s transmission region to move a little around the wavelength of Na D<sub>2</sub> between two successive scans was taken into account (1) by using a flat-field scan which covers a significantly larger spectral range than any single solar scan and (2) by determining meticulously for each individual scan of the time series which part of the flat-field scan matches it in wavelength. This was done by first averaging intensities over a suitable small area around the optical axis in the images of each narrow-band scan. A curve is thus obtained which contains the averaged line profile of Na D<sub>2</sub>. This curve was then divided by the averaged transmission curve of the artificial flat-field scan. The procedure usually had to be repeated several times by “shifting” these curves, the averaged curve and the transmission curve, against each other in wavelength until the resulting line profile closely resembled the exemplary profile from a standard atlas of the solar spectrum. Usually, the best results could only be achieved after some interpolation between the flat-field images, thus allowing finer wavelength steps. With the results from the averaged curves, the individual images of each solar scan were correspondingly divided by the matching images of the flat-field scan.

The necessary corrections for image motion and distortions were then applied to the narrow-band filtergrams by perfect

analogy with the results obtained from the correlation of the corresponding white-light images taken simultaneously.

Compensation for the blueshift of the profiles (see Sect. 2.2) was achieved by dividing the *flat-field scan obtained with solar light* by the artificial flat-field scan, where care was taken again that the individual images used for division corresponded to the same wavelength. Thus, for every pixel in the field of view, a line profile resulted. The position of every line (intensity) minimum was determined by a fourth-order polynomial fit. With these values, an array was created giving the amount of wavelength shifts according to the pixels' position in the field of view. This array was employed to correct the individual line profiles of every pixel in every scan of the time series for the blueshift due to the FPI's position at the pupil's image.

Finally, noise in the data cube (one spectral and two spatial dimensions) was reduced by using a three-dimensional optimum filter in the Fourier domain.

### 3.4. New images

The proper ingredients of diagnostic diagrams are “minimum (intensity) images” and velocity maps. For the first type of images, the minimum intensity of each profile in the field of view was calculated using fourth-order polynomial fits to the immediate neighbourhood of the line core (i.e.  $\pm 120$  mÅ around the line minimum) to avoid “photospheric contamination” by contributions from the line wings. The velocity fields were derived from the Doppler shifts of the profiles which had been determined from the positions of the line minima represented by the polynomial fits as well. The “image numbers” of a scan also give a wavelength scale as the spectral difference between neighbouring images was chosen to be 30 mÅ.

The minimum images had to be correlated with each other and needed to be intensity-scaled in the same way as the reference white-light images whereas for the velocity maps, evidently only the correlation was necessary.

An example of small subfields of minimum images is given in Fig. 3.

Finally, the criterion used to discriminate between the intra-network and the network regions (the comparison between which will become of some importance in the following section) should be mentioned in this context: The averaged minimum intensity image which was obtained from all 128 minimum images shows bright parts, presumably bordering a supergranule (with a typical diameter of about  $40''$ ), and darker ones which were considered to belong to the intra-network. Whenever no clear distinction between the two seemed possible (here, the averaged minimum image prompted an intensity range from about 2.7% to 3.5% above the mean intensity  $\bar{I}_{\min}$ ), the corresponding regions were totally neglected. At first sight it might be confusing that the intensity limit for the intra-network ( $\leq 2.7\%$  above  $\bar{I}_{\min}$ ) also lies above the mean intensity, but this is simply a consequence of the intensities in the intra-network regions fluctuating around some lower value than  $\bar{I}_{\min}$  (as to be expected), and thus surpassing it in some areas. Most intensity values in the

network exceeded  $\bar{I}_{\min}$  considerably, especially for those areas persisting throughout the whole observing period.

According to the criterion given here, the intra-network covered about four times the size of the network areas.

### 3.5. Diagnostic tools

In the next step, one- and two-dimensional power, phase, and coherence spectra were computed. Although under certain conditions, it is possible to obtain  $V-V$  and  $I-I$  phase spectra from only one spectral line (using “fixed” positions in the line wings as well, see e.g. Deubner et al. (1996)), the observed set of data was best suited to yield  $V-I$  phase spectra, i.e. the phase differences between the Doppler shifts of the line cores and the line-centre intensities as a function of frequency and, in the two-dimensional case, of wavenumber which was taken as an average over suitable intervals in the  $k_x-k_y$  plane. Because of the apodization necessary in the Fourier transform which had been performed before, 5 pixels from each border of the images were lost, so that the resolution in wavenumber was slightly deteriorated. As an area of  $69.4 \times 50.4$  corresponds to  $50.315$  Mm  $\times$   $36.54$  Mm on the solar surface, the resolution was limited in one spatial dimension by  $\Delta k_x \approx 0.125$  Mm $^{-1}$  and by  $\Delta k_y \approx 0.172$  Mm $^{-1}$  in the other.

The temporal Nyquist frequency of (only) about 8.9 mHz naturally suggests a practical improvement if the two-dimensional spectrometer were to be used regularly for observing solar oscillations. With faster PCs and enhanced disk storage it would be possible to take successive scans in shorter intervals and get even longer time series to improve the resolution in frequency (which is 0.14 mHz here). Nevertheless, as the following section shall show, the concept devised for this observation has proved a fairly good compromise.

## 4. Results and discussion

### 4.1. One-dimensional power, coherence, and phase spectra

The first approach to the chromospheric oscillations measured in the Na D<sub>2</sub> line was made by plotting one-dimensional power spectra averaged over the whole field of view, but also separately for network and intra-network regions (see Fig. 1). However, as the same field of view was retained throughout the time series, this comparison may not yield a really representative result due to the relatively low statistical weight of the data. Yet, it is surprising that neither in the power spectrum derived from the Doppler shifts nor in another one derived from fluctuations of the line-centre intensity pronounced differences were found between the three curves.

In the upper panel of Fig. 1, the power maximum lies around 3.3 mHz for the network, corresponding to the well-known 5-minute oscillations. It is remarkable, though, that for the intra-network, the maximum is just slightly shifted towards higher frequencies. The latter power curve does not rise for frequencies higher than 3.3 mHz to indicate maximum power for about 5 – 5.5 mHz (corresponding to periods between 180 and 200 s)

which was reported by numerous observers from other chromospheric lines (Lites et al. 1993; Bocchialini et al. 1994; von Uexküll & Kneer 1995). An explanation for the comparatively weak power in the 5 – 5.5 mHz frequency range would be a lower line formation height of  $\text{Na D}_2$  than previously adopted. This hypothesis is supported by a similar finding of Kneer & von Uexküll (1993) for the  $\text{Mg b}_2$  line which is formed in the *lower* chromosphere (see e.g. Schmieder (1979), Staiger (1985) or Deubner et al. (1990)) and does not show maximum power from oscillations with periods of about 3 minutes, either. Besides, like for  $\text{Na D}_2$ , the power curves did not indicate any marked differences between the network and the intra-network regions. Although as yet, the determination of the individual line formation heights is too complicated to yield definite results, there still seems to be an agreement on the *relation* of these heights: The  $\text{Mg b}_2$  line is formed lower in the solar chromosphere than  $\text{Na D}_2$ , but the latter line formation height might not lie as high as about 1000 km above the level where  $\tau_{5000} = 1$  which was inferred e.g. from Gehren (1975) and from Caccin et al. (1980). From a number of further publications, one may conclude as well that  $\text{Na D}_2$  is formed somewhat lower in the chromosphere, but, of course, still higher than the  $\text{Na D}_1$  line. Fleck & Deubner (1989) also mentioned this relation and assumed a line formation height of about 800 km for  $\text{Na D}_1$  which Staiger (1987) previously stated to be 760 km. The results presented here give rise to some speculation about the exact formation height indeed. Although they are not suitable to settle this question, they may serve to narrow down the plausible height range. At least, they strongly suggest that its *upper* limit does not reach the highest estimates quoted above. Sect. 4.2 will provide some clues as to the equally important problem of the *lower* limit, from which not too precise a conclusion, yet a safe one, can be drawn: All results are consistent with the assumption that  $\text{Na D}_2$  is formed somewhere in the lower to middle chromosphere. As this piece of information is anticipated here, the question of the line formation height need not be resumed every time this topic is touched again in the discussion of further results.

The power spectra in the lower panel of Fig. 1 were obtained from the fluctuation of the line-centre intensity, but otherwise they correspond to those in the upper panel. As in the course of the Fast Fourier Transform (FFT) the average intensity or velocity, respectively, was subtracted from the data, *all* power spectra presented here drop to zero at 0 mHz, whereas a *real* common feature in both panels is the enhanced power in the frequency range from about 2 to 6 mHz for network as well as for intra-network areas. Yet the enhancement in the lower panel is small compared to the power maximum around 0.15 mHz, contrary to the situation shown in the upper diagram.

Even though the position of this low-frequency maximum in the power spectra in both panels is not related to any periodic process on the Sun but is given by the length of the underlying data set (a time series or “period” of nearly 2 hours is equivalent to a frequency of about 0.15 mHz), there is a physical explanation for the substantial increase of this maximum in the lower panel, which is illustrated by Figs. 2 and 3.

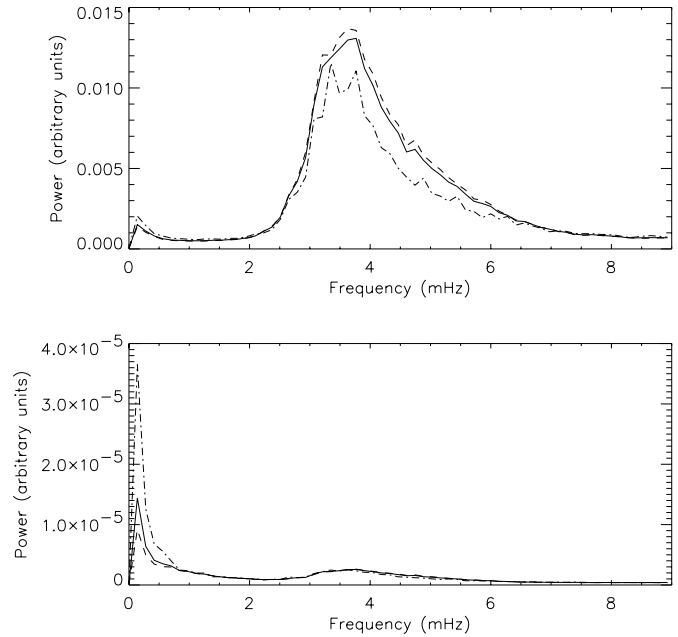


**Fig. 1.** One-dimensional mean power spectra — upper panel: derived from Doppler shifts, lower panel: derived from the fluctuation of the line-centre intensity (the dashed line refers to the intra-network, the dash-dotted line to network regions, the solid line represents the power spectrum for the whole field of view)

Evidently, the low-frequency power is much higher for network than for intra-network regions. Fig. 2 gives three examples of the temporal behaviour of the line-centre intensity of small network areas where the line-centre brightness slowly decreases while the amplitude of the intensity fluctuation remains nearly the same over 2 hours. It was checked by the white-light images of the time series, too, that seeing effects could only have had a minor influence on these curves. Therefore, the interpretation suggests itself that here, the (perhaps only short-term) fading of network regions is monitored, as the line-centre intensity of the network approaches the value of the surrounding intra-network. On the other hand, there were also network regions with slowly increasing (while “rapidly” fluctuating) minimum intensity which point to a strengthening of network boundaries. Thus, both the enhancement and the fading of network regions obviously occur only locally, and both processes leave their traces in the corresponding power spectrum of Fig. 1 forming low-frequency maxima.

Fig. 3 shows the temporal development within a subfield of the minimum images which contains the “pure” network region, whose fluctuation of the line-centre intensity is shown in the upper panel of Fig. 2, and the surrounding intra-network within a field of view of  $14'' \times 15''$ . Here, time proceeds row by row with a distance of 56 s between successive images. The network boundary is (mostly) seen here as an almost vertical bright streak. At the beginning of the observing run and also during the second half of the time series, the appearance of this part of the network was changing significantly. As already mentioned, seeing effects did not contribute much to its rather

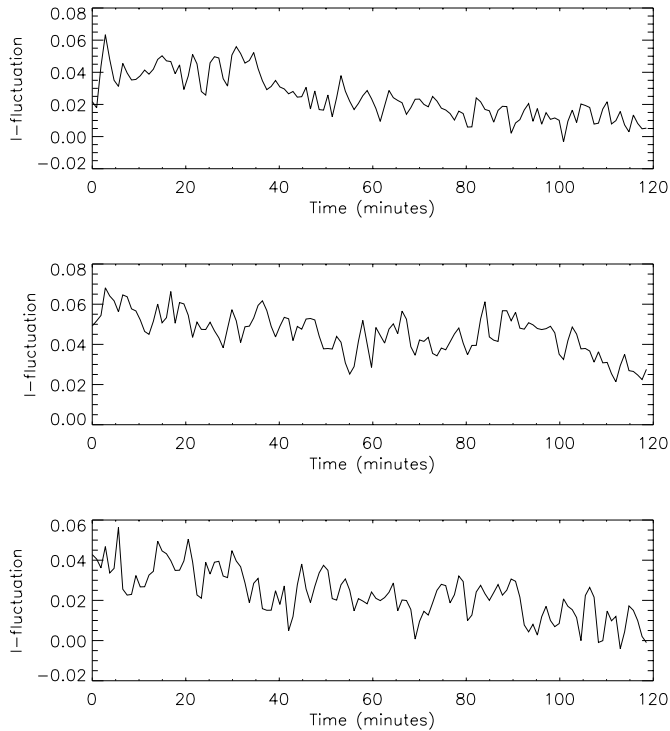


**Fig. 2.** Temporal development of the fluctuation of the line-centre intensity for three distinct small areas from the network

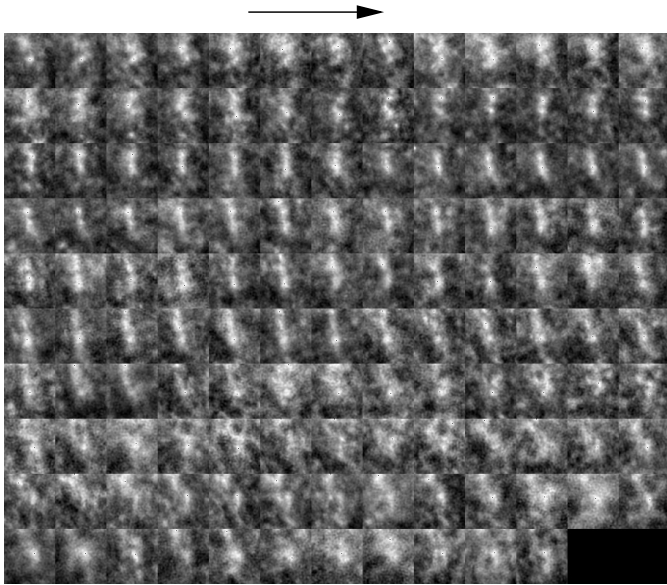


**Fig. 3.** Temporal development of a small network region in a ( $14'' \times 15''$ ) subfield of the minimum images

diffuse appearance towards the end of the observation. Hence, this sequence of minimum images can be trusted to reflect the real changes within the solar atmosphere.

Fig. 4 represents the one-dimensional V–I coherence and phase spectra of the Na D<sub>2</sub> line, obtained from the whole field of view. In the frequency range between 0 and 0.8 mHz, the phase reaches about  $-160^\circ$  which might be due to supergran-

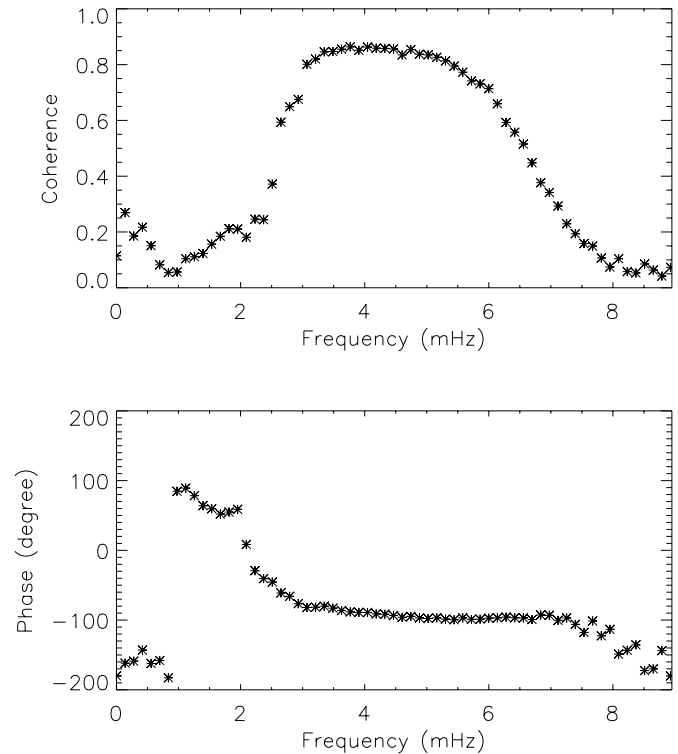


**Fig. 4.** One-dimensional V–I coherence and phase spectra derived from the Na D<sub>2</sub> line over the whole field of view

ular flows, as there is an anti-correlation between blueshift and brightness. The  $70^\circ$  plateau between 0.8 and 2 mHz seems to be a new discovery in *chromospheric* V–I phase differences. Nevertheless, an explanation for this plateau was already found some time ago. As the two-dimensional phase spectrum yields more detailed information and the plateau is also seen there, it will be treated in the next subsection. A discussion of the change of sign with decreasing frequency at about 2.1 mHz from negative to positive values which was also found in the phase spectra of Schmieder (1976), Lites & Chipman (1979), and Staiger et al. (1984) will follow in Sect. 4.2 as well.

In the evanescent range, between 3 and 5 mHz, where the coherence is as high as 0.8, the phase difference is  $-90^\circ$ , as predicted by theory. In the acoustic domain, between 5 and 7.5 mHz, the coherence decreases from high values down to 0.15. Here, the phase difference is still  $-90^\circ$  on the average and thus suggests standing waves without necessarily being an indication of them. A similar behaviour was also found in the V–I phase spectra of the Ca II line at  $8498 \text{ \AA}$  and Na D<sub>1</sub> and has been interpreted as the signature of standing waves indeed (Fleck & Deubner 1989). However, it is important to note that these one-dimensional spectra just represent the case of the corresponding two-dimensional  $k$ – $\omega$  diagrams integrated over the horizontal wavenumber  $k$ . The phase differences found here thus result from a mixture of waves with various wavenumbers. The two-dimensional phase spectrum treated in Sect. 4.2 therefore provides a better basis for further analysis.

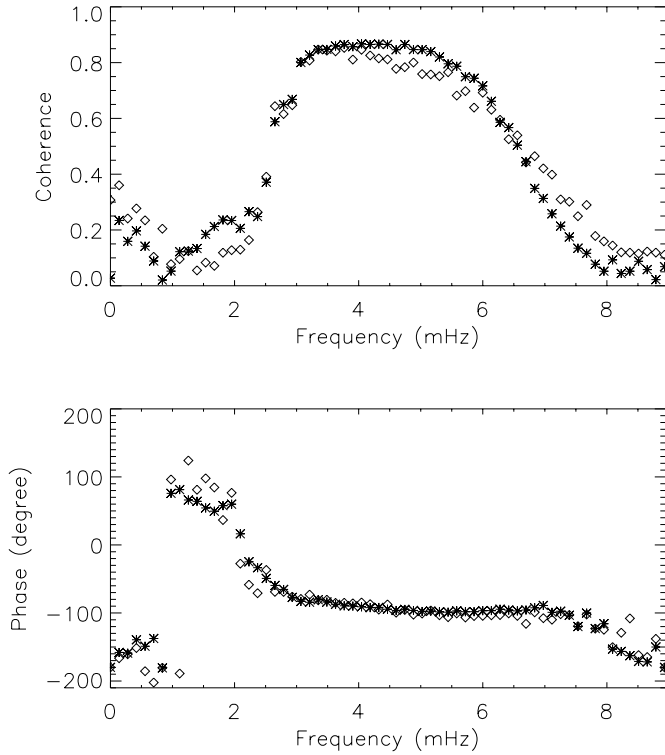


**Fig. 5.** One-dimensional V–I coherence and phase spectra for the intra-network (asterisks) and for the network (diamonds)

Contrary to other observations, a phase jump of  $\pm 180^\circ$  at about 8 mHz is *missing* here. It was observed for the first time by Staiger et al. (1984) and later on, Fleck & Deubner (1989) also found one in the Na D<sub>1</sub> line at  $\mu = 0.8$ , whereas at the centre of the solar disk ( $\mu = 1$ ), they observed a phase jump of only about  $90^\circ$  in Na D<sub>1</sub> which they considered to be “incomplete”. However, in Fig. 4, the phase values just slowly decrease with some scattering from 7.5 mHz on. There is no indication of any phase jump at all. Yet, this does not necessarily mean that for Na D<sub>2</sub>, a phase jump really does not occur, as the Nyquist frequency for the data set presented here is only 8.9 mHz, and aliasing might have affected this result. At the expense of “true” two-dimensional recording of their data set, Deubner et al. (1996) obtained a time series in Na D<sub>2</sub> with a much higher Nyquist frequency of 20 mHz, using the so-called lambdameter method for their analysis. Their V–I phase spectra displayed again a phase jump of  $180^\circ$  near 8 mHz. This discontinuity is best seen in two V–I phase spectra from two positions a little higher up in the Na D<sub>2</sub> profile than the very line core. The lambdameter method also allowed them to derive V–V spectra from only one Fraunhofer line, i.e. from different positions within the line profile corresponding to different atmospheric heights. Surprisingly, the V–V spectra of Na D<sub>2</sub> revealed another  $180^\circ$  phase jump at about 7 mHz, belonging to adjacent positions considerably higher in the line profile or, correspondingly, much lower in the solar atmosphere than in the case of the V–I phase spectra. The phase jump in the V–V spectra was claimed to be the first one of this kind ever seen. Deubner et al. explained their

combined findings by a three-component wave field meeting several specific requirements.

The one-dimensional V–I coherence and phase spectra for the intra-network and for the network regions (see Fig. 5) look similar to those for the entire field of view. Only the scattering of phase values for the network boundaries (e.g. between 1.1 and 2.4 mHz) is somewhat more pronounced, thus, in some frequency intervals, the coherence is lower than for the intra-network. This enhanced scattering might simply be accounted for by the smaller number of pixels belonging to network regions in the field of view (20 % of all pixels considered, cf. Sect. 3.4).

#### 4.2. Two-dimensional diagnostic tools

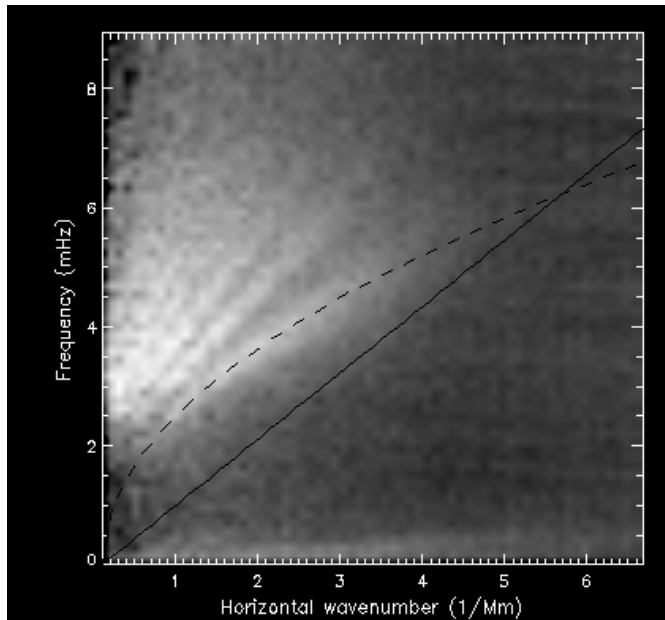
The two-dimensional power spectrum in Fig. 6 was derived from the oscillation of the Doppler shifts of Na D<sub>2</sub>. The solid line indicates the Lamb mode ( $\omega_l = c_s k$ , where  $7 \text{ km s}^{-1}$  was adopted for  $c_s$ , and  $k = (\text{horizontal})$  wavenumber) and the dashed line marks the f-mode ( $\omega_f = \sqrt{g k}$  with  $g = 274 \text{ m s}^{-2}$ ).

The p-modes can be distinguished separately from p<sub>0</sub> (or f-mode), extending to a horizontal wavenumber of about  $4 \text{ Mm}^{-1}$ , to p<sub>5</sub>. The p-modes reach to higher frequencies than the acoustic cut-off frequency ( $\sim 4.7 \text{ mHz}$ ) and thus show “pseudo-ridges” (see Kumar & Lu (1991)) which are also seen in other chromospheric  $k$ – $\omega$  diagrams (e.g. Fernandes et al. (1992)).

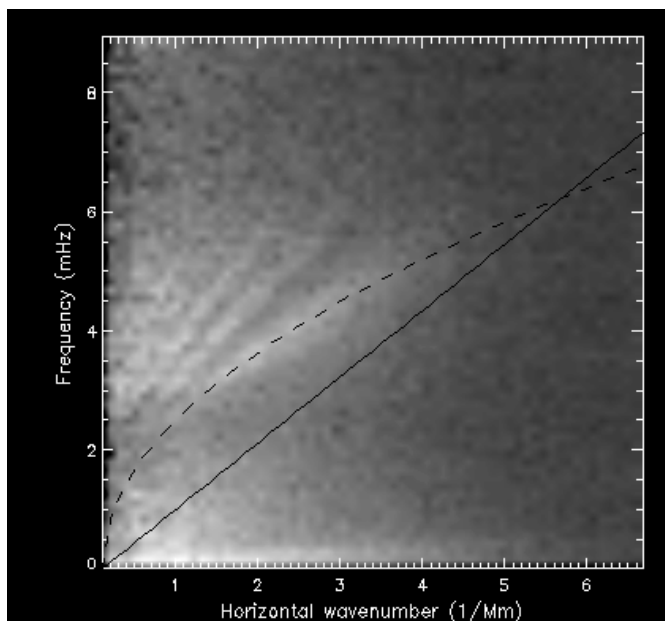
A most remarkable result of Fig. 6 is the *missing* hint of a chromospheric eigenmode which in case of existence would have shown as a horizontal bright streak in the frequency range from about 5 to 5.5 mHz (corresponding to 3-min oscillations). Ulrich & Rhodes (1977) predicted a frequency of 5.6 mHz for such a mode from theoretical calculations. Steffens et al. (1995) report enhanced power *between* the ridges near the cut-off frequency at 5.6 mHz which might be an indication of a “chromospheric ridge”.

Fig. 7 displays a two-dimensional power spectrum obtained from the fluctuation of line-centre intensities. Here, too, the ridges corresponding to p<sub>0</sub> up to p<sub>5</sub> appear, but with somewhat poorer contrast than in Fig. 6. Yet, the extension of the f-mode to a wavenumber of  $4 \text{ Mm}^{-1}$  and of the pseudo-modes to about 6 mHz in frequency is still discernible. Fig. 7 gives no hint of a chromospheric eigenmode either, but it shows a striking region of enhanced power in the low-frequency range below 1.5 mHz and limited in wavenumber to below about  $2 \text{ Mm}^{-1}$ . This enhancement might be due to the strengthening or fading of the network, and, possibly, to gravity waves.

The V–I coherence and phase spectra of Na D<sub>2</sub> are represented by Figs. 8 and 9. In the first one, a region of very high coherence extends from the domain of 5-min oscillations over the acoustic cut-off frequency to about 6.5 to 7 mHz. In the inter-ridges, the coherence drops a little, thus revealing the ridges from p<sub>0</sub> to p<sub>2</sub>. Below the Lamb frequency in the domain of gravity waves, the coherence decreases from about 0.8 to even below 0.4. Only in a small area below 0.5 mHz and between 1.3 and 2.3  $\text{Mm}^{-1}$  it takes high values again. In another area limited by the Lamb mode and by the f-mode where frequencies are lower than about 2 mHz, the coherence is also



**Fig. 6.** Two-dimensional power spectrum of  $\text{NaD}_2$  oscillations derived from Doppler shifts; the solid line represents the Lamb mode, the dashed curve indicates the f-mode



**Fig. 7.** Two-dimensional power spectrum of the line-centre intensity fluctuation of the  $\text{NaD}_2$  line

remarkably high. The phase values corresponding to this region are *positive*, as can be seen in Fig. 9. This outcome is baffling enough as an evanescent wave domain is expected to show a phase difference of  $-90^\circ$ . The one-dimensional V–I spectrum also shows a “plateau” with phase values of about  $70^\circ$  (cf. Sect. 4.1) whose origin may now be understood as being due to the positive phase differences in the region between the Lamb and the fundamental mode as well. The transition from this plateau to the evanescent region causes the phase discontinuity seen at

2.1 mHz. Some similar results showing phase discontinuities in V–I spectra at about 2 mHz, though in *photospheric* lines, have been reported previously (Lites & Chipman 1979; Staiger et al. 1984; Deubner et al. 1990). As thus the same problem has been encountered with lines which are supposed to have formed in quite different layers of the solar atmosphere, it is once again tempting to explain this finding by a lower line formation height of  $\text{NaD}_2$  than was first assumed here. There are indeed some authors who consider  $\text{NaD}_2$  to possibly originate from the upper photosphere (e.g. Babij & Stodilka (1987), Espagnet et al. (1995) or Kariyappa (1996)), but these new results do not support such a low formation height. Several typical features found in the V–I phase spectra of lines formed in the upper photosphere like, for instance, the extension of the plateau showing positive phases into the inter-ridge area between the p-modes and others quoted by Deubner et al. (1996) cannot be seen in Fig. 9. Therefore, the lower chromosphere seems to be a good estimate of the lower limit of the line formation height of  $\text{NaD}_2$ .

Hence, it was not expected beforehand that the above-mentioned phase discontinuities would also appear in the line under consideration. A solution to this problem proposed by Marmolino & Severino (1991) was actually based on an earlier work by Souffrin (1966) and a related contribution by Mein (1966). According to their investigation, to compensate for the loss of energy by radiative damping, running waves, which are capable of propagating energy, appear in the evanescent regime of the  $k$ – $\omega$  diagram. This explanation may well apply here.

There is another small region deserving attention which was already mentioned above. Below 0.5 mHz and between 1.3 and  $2.3 \text{ Mm}^{-1}$  high coherence (0.8 to 0.9) is found. Phase differences in this area marking the domain of gravity waves are about  $-160^\circ$ . At first sight, one might suspect convective supergranular flows to be responsible, but the typical size of a supergranule (about  $40''$ ) corresponds to a wavenumber of  $0.216 \text{ Mm}^{-1}$  and thus fails to explain the high coherence between 1.3 and  $2.3 \text{ Mm}^{-1}$ . Mesogranules do fit in this wavenumber range, but they have not been observed in the minimum images (showing the line-centre intensities) and thus cannot account for the coherence, either. Therefore, it seems plausible that gravity waves left their mark in these diagrams. Kneer & von Uexküll (1993) found a region of high coherence in their I–I phase spectrum between  $\text{Mg b}_2$  and Ca K below 1.59 mHz and between 1 and  $2 \text{ Mm}^{-1}$  which they also attributed to gravity waves.

The high coherence values below about  $0.5 \text{ Mm}^{-1}$  showing in the low-frequency range of Fig. 8, though, may well be connected with convective flows.

The two-dimensional phase spectrum exhibits a remarkable behaviour in the decrease of phase differences from about  $-60^\circ$  for the f-mode to about  $-120^\circ$  for higher modes. This finding still lacks an explanation. It should be mentioned in this context that according to Kumar & Lu (1991) pseudo-modes (i.e. running acoustic waves) are supposed to show a V–I phase difference of  $0^\circ$ . Here, as a possible interpretation one may assume the signals for the fluctuation of the Doppler shifts (velocity) and for the intensity to originate from different atmospheric heights. For spectral lines like  $\text{NaD}_2$  and similar chromospheric lines

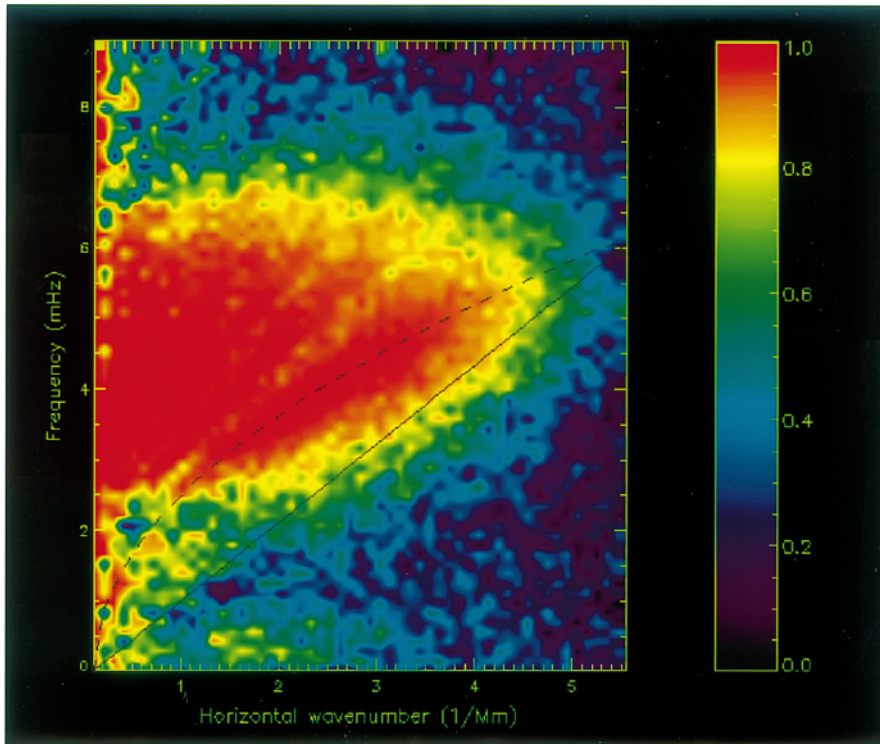


**Fig. 8.** Two-dimensional V–I coherence spectrum (solid line: Lamb mode, dashed curve: f-mode); the colour bar to the right of the diagram indicates the coherence values

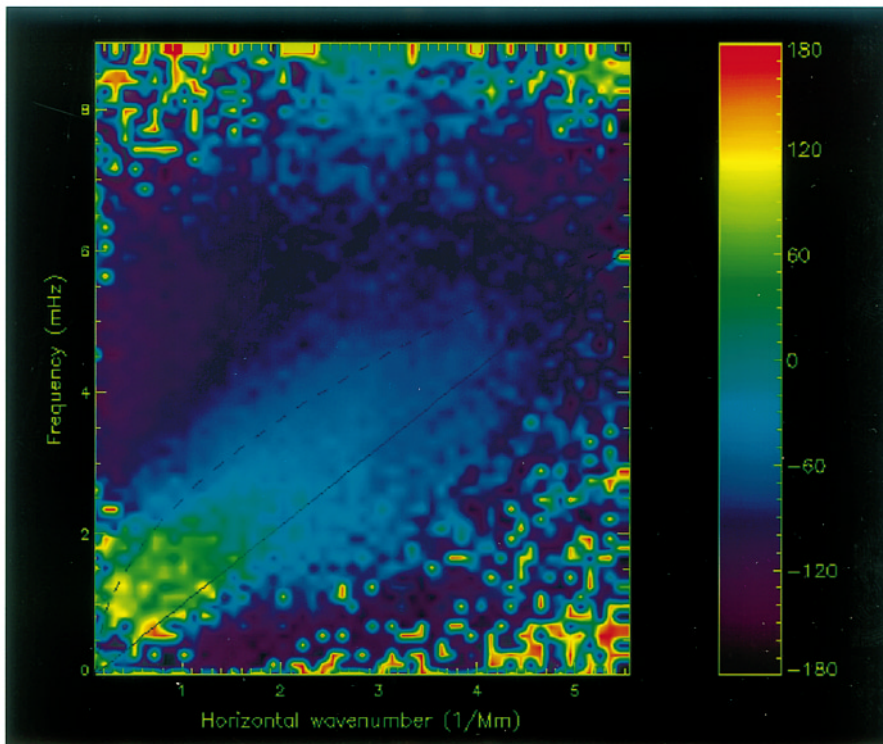


**Fig. 9.** Two-dimensional V–I phase spectrum; for each colour, the corresponding phase (degree) is given by the colour bar

which are not formed in the local thermodynamic equilibrium (LTE) the velocity signal represents higher layers than the intensity signal. As a consequence, acoustic waves running upwards show an increasing “distance” between the intensity and the velocity signal with increasing frequency. This explanation may well be valid for either one of the Na D lines which are radiation-

dominated, but the situation is different for collision-dominated chromospheric lines like, for example, Ca II K, 8542, and 8498. Mein & Mein (1980) have computed the formation heights of velocity and intensity for the latter lines and found the distance of the two heights decreasing in the order of decreasing line strength, i.e. as collisions become more frequent for Ca II 8542

and 8498 than for Ca II K (which means that the weaker Ca II lines get closer to LTE conditions).

It appears to be useful to recall that these results are not applicable to the Na D<sub>2</sub> line whose behaviour, however, might finally be explained by models of wave propagation which also consider radiative transport.

## 5. Summary and outlook

To provide a better overview, the results discussed in the previous section are summarized here:

- The power spectra obtained separately from the intranetwork on the one hand and from the network on the other differ conspicuously little, while other observers using different chromospheric lines found different oscillation periods in their respective power spectra. Here, both regions show enhanced power in a frequency range between 2 and about 6 – 6.5 mHz. This result was derived from Doppler shifts.
- The corresponding power spectra derived from the fluctuation of the line-centre intensity also show increased power in roughly the same range, but here, the network regions produced a much higher power maximum around 0.15 mHz which is mostly due to the formation of new network regions and also to the fading of some parts of the existing network.
- The temporal development of the fluctuation of the line-centre brightness was monitored and clearly supports the explanation given above.
- The phase jump at about 8 mHz found by some observers in one-dimensional V–I phase spectra could not be confirmed here. The missing phase jump might be due to aliasing as the Nyquist frequency is only 8.9 mHz here, yet from these Na D<sub>2</sub> data, it cannot be excluded that this jump really does not occur.
- Neither the two-dimensional power spectrum computed from the Doppler shifts of the line cores nor the corresponding spectrum from the intensity fluctuation of the line minimum gives a clue to a chromospheric eigenmode. In case of existence, it should have produced a horizontal bright streak between 5 and 5.5 mHz.
- Below 2 mHz and bordered by the Lamb and the f-mode, a plateau of phase values around 70° was found in the two-dimensional V–I phase spectrum which can be explained by the dispersion relation for evanescent waves with upward propagating energy.
- The two-dimensional V–I phase spectrum possesses an isolated region of high coherence for less than 0.5 mHz and between about 1.5 and 2.5 Mm<sup>-1</sup>, to a high degree of probability representing the signature of gravity waves in the line formation height of Na D<sub>2</sub>.
- The decrease of phase differences seen in the two-dimensional phase spectrum from about –60° for the f-mode to about –120° for higher modes is still puzzling. A tentative explanation is given in Sect. 4.2, a better supported one may finally follow from model calculations of wave propagation with due consideration of radiative transport.

The investigation of the oscillatory behaviour of the solar chromosphere will continue to profit from further observations. In principle, data from only one spectral line do not suffice for a proper study of e.g. the propagation of energy. More detailed knowledge would rather be obtainable from V–V or I–I spectra of two different spectral lines forming in different chromospheric heights. Major steps towards a better understanding of chromospheric oscillations can therefore be expected from simultaneous *two-dimensional* observations in such lines. For some time to come, this will remain a challenge to the development of even more powerful and versatile instruments than presently available.

*Acknowledgements.* This work was supported by a scholarship from the University of Istanbul. Thanks are due to R. Volkmer and S. Steffens for their assistance with the data reduction and for valuable discussions. The co-operation of C. Denker and J. Krieg in obtaining the observations is gratefully acknowledged. The Vacuum Tower Telescope at the Spanish Observatorio del Teide of the Instituto de Astrofísica de Canarias/Tenerife is operated by the Kiepenheuer-Institut für Sonnenphysik in Freiburg, Germany.

## References

- Al N., 1997, Thesis, University of Göttingen  
 Babij B.T., Stodilka M.I., 1987, Sol. Danny Bull. 11, 80  
 Bendlin C., 1993, Thesis, University of Göttingen  
 Bendlin C., Volkmer R., 1995, A&AS 112, 371  
 Bendlin C., Volkmer R., Kneer F., 1992, A&A 257, 817  
 Bocchialini K., Vial J.-C., Koutchmy S., 1994, ApJ 423, L67  
 Caccin B., Gomez M.T., Roberti G., 1980, A&A 92, 63  
 Deubner F.-L., 1975, A&A 44, 371  
 Deubner F.-L., Fleck B., Marmolino C., Severino G., 1990, A&A 236, 509  
 Deubner F.-L., Waldschik Th., Steffens S., 1996, A&A 307, 936  
 Espagnet O., Muller R., Roudier Th., Mein N., Mein P., 1995, A&AS 109, 79  
 Fernandes D.N., Scherrer P.H., Tarbell T.D., Title A.M., 1992, ApJ 392, 736  
 Fleck B., Deubner F.-L., 1989, A&A 224, 245  
 Gehren T., 1975, A&A 38, 289  
 Kariyappa, R., 1996, Solar Physics 165, 211  
 Kneer F., von Uexküll M., 1993, A&A 274, 584  
 Kumar P., Lu E., 1991, ApJ 375, L35  
 Leighton R.B., Noyes R.W., Simon G.W., 1962, ApJ 135, 474  
 Lites B.W., Chipman E.G., 1979, ApJ 231, 570  
 Lites B.W., Rutten R.J., Kalkofen W., 1993, ApJ 414, 345  
 Marmolino C., Severino, G., 1991, A&A 242, 271  
 Mein N., Mein P., 1980, A&A 84, 96  
 Mein P., 1966, Ann. Astrophys. 29, 153  
 Schmieder B., 1976, Solar Phys. 47, 435  
 Schmieder B., 1979, A&A 74, 273  
 Schwarzschild M., 1948, ApJ 107, 1  
 Souffrin P., 1966, Ann. Astrophys. 29, 55  
 Staiger J., 1985, Thesis, University of Freiburg i. Br.  
 Staiger J., 1987, A&A 175, 263  
 Staiger J., Schmieder B., Deubner F.-L., Mattig W., 1984, Mem. Soc. Astron. Ital. 55, 147  
 Steffens S., Deubner F.-L., Hofmann J., Fleck B., 1995, A&A 302, 277  
 Ulrich R.K., 1970, ApJ 162, 993  
 Ulrich R.K., Rhodes E.J., 1977, ApJ 218, 521  
 Volkmer R., 1995, Thesis, University of Göttingen  
 von Uexküll M., Kneer F., 1995, A&A 294, 252